Modeling Multiphase Effects in the Combustion of HMX and RDX

Ephraim B. Washburn*
Naval Air Warfare Center Weapons Division, China Lake, California 93555
and
Merrill W. Beckstead†
Brigham Young University, Provo, Utah 84602

Hexahydro-1,3,5-trinitro-1,3,5-triazine (RDX) and octahydro-1,3,5,7-tetranitro-1,3,5,7-tetrazocine (HMX) have similar structures and burning rates. However, the burning-rate temperature sensitivity (σ_p) is significantly different between RDX and HMX at low pressures. Recent efforts to mathematically model the steady-state combustion of RDX and HMX with detailed chemical kinetics in the gas phase and distributed decomposition in the condensed phase have succeeded in modeling burning rates at a specific initial temperature. However, all have underpredicted the σ_p trends of HMX at low pressure and have not differentiated the σ_p of RDX and HMX. RDX and HMX both burn with a thin multiphase surface of bubbles in liquid. A liquid–bubble submodel was developed to improve σ_p calculations. To predict the observed HMX σ_p values with the model, first, evaporation in the subsurface was limited near the gas/liquid surface. Second, the difference in surface temperature at different initial temperatures was adjusted to follow trends in experimental data. Third, the Marangoni effect was added to the calculation of the bubble velocities. For RDX, there was little change in the calculated σ_p values with the addition of the liquid–bubble submodel.

Nomenclature

C_D	=	drag coefficient
C_P	=	specific heat capacity
C_{VM}	=	virtual-mass coefficient
D	=	diameter
F	=	force
f_2	=	fugacity
H_f	=	heat of formation
H_{pc}	=	heat of phase change
M	=	mass flux
P	=	pressure
q_{evap}	=	evaporation rate at surface
Re	=	Reynolds number
r	=	dT_s/dT_o
T	=	temperature
T_m	=	melt temperature
u	=	velocity
V	=	volume
X	=	mole fraction
Xsol	=	solubility mole fraction
x	=	distance
γ	=	activity coefficient
λ	=	thermal conductivity
μ	=	viscosity
ρ	=	density
σ	=	surface tension
σ_p	=	burning-rate temperature sensitivity
ϕ	=	void fraction

Subscripts

B	=	buoyancy
bub	=	bubble
crit	=	critical
D	=	drag
g	=	gas
k	=	species index
l	=	liquid
MG	=	Marangoni effect
o	=	initial
s	=	surface
VM	=	virtual mass

*Chemical Engineer, Energetics Research Division, MS 6204; Ephraim. Washburn@navy.mil. Member AIAA.
†Professor, Chemical Engineering Department, 350 CB. Associate Fellow AIAA.

Introduction

THE propellant and explosive ingredients, hexahydro-1,3,5-trinitro-1,3,5-triazine (RDX) and octahydro-1,3,5,7-tetranitro-1,3,5,7-tetrazocine (HMX), have similar structures (RDX has one less repeating CH_2NNO_2 unit), burning rates, and final flame temperatures. During steady-state combustion, both have a solid-phase region with a thin molten layer followed by a gas-phase region where most of the heat release occurs (see Fig. 1). A difference between HMX and RDX is that HMX has a higher surface temperature and should, therefore, have more condensed-phase decomposition. Also, at low pressure HMX has a greater burning rate, especially at higher initial temperatures.

As early as 1950, Parr and Crawford proposed a model for double-base propellant that included distributed combustion (combustion throughout a region instead of isolated to a surface) in the molten condensed phase [1]. Their one-dimensional, steady-state physical model consisted of three zones: a foam reaction zone, a fizz reaction zone, and a flame reaction zone. In the foam reaction zone, the energy equation was solved with a global condensed-phase reaction mechanism with one solid reactant converting to one gaseous product (i.e., the foam reaction). A weighting function was used for foam zone density to account for the disparity between the solid and gas density.
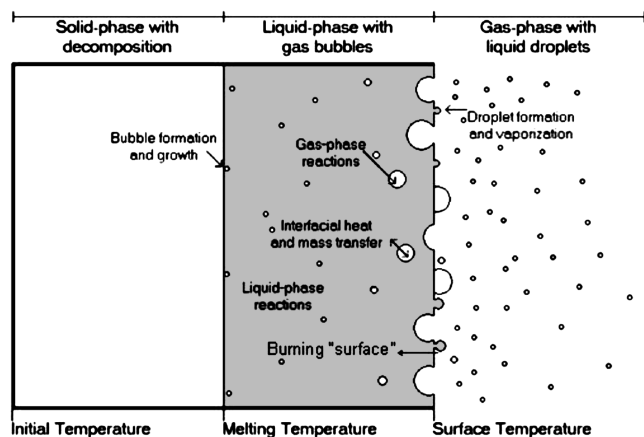
Fig. 1 Physical picture of nitramine steady-state combustion.

Similar models were proposed for the fizz and flame reaction zones [2,3], yet Parr and Crawford differed in their treatment of the foam or condensed phase. The other models of the condensed phase in the early 1950s included only a global surface reaction. The lack of computational power led to assumptions of constant solid properties and global reaction mechanisms. Only approximate analytical solutions were obtained.

In 1966, Hermance proposed a composite propellant combustion model. His model described a solid region and two gas regions [4]. Hermance did not include distributed combustion in the condensed phase, but assumed that the condensed-phase reaction occurred at the surface. The contribution of Hermance was the inclusion of multiple reactant and product species in the condensed phase.

During the 1970s several models for propellant combustion were developed and were summarized by Beckstead and McCarty [5] and by Cohen [6]. The advancements in the propellant ingredient models from the 1970s were primarily in the gas-phase description. Virtually all the propellant ingredient models used an Arrhenius expression for a single reaction at the propellant surface to describe the condensed-phase decompostition.

During the late 1970s and early 1980s Ben-Reuven et al. [7,8] published their flame and subsurface deflagration model for RDX and HMX. They included one global reaction step for the liquid decomposition that resulted in four product species. Their temperature and species reaction equations were essentially identical to those of Parr and Crawford. Ben-Reuven et al. accounted for the change in density that accompanies the liquid decomposition with the same relationship used by Parr and Crawford [7,8].

The new contributions added by Ben-Reuven et al. were their inclusion of a reaction with multiple products in the liquid phase and their treatment of the boundary conditions. They assumed that decomposition occurred after the monopropellant melted. Therefore, they started their calculations at the melt temperature with a monopropellant mass fraction of one. The heat flux boundary condition across the solid/liquid surface was set to the sum of the flux needed to melt the propellant plus the flux needed to heat the solid from the initial temperature to the melting temperature. With the two differential equations and the boundary conditions, they integrated the equations until a prespecified surface temperature was reached.

In 1987 and 1990 Williams et al. [9–11] published models for nitramine deflagration. Their models involved a melt layer either decomposing to gaseous product or vaporizing to gaseous reactant. The energy equation resembles the equation used by Parr and Crawford, but the source term is expanded. A multistep condensed-phase chemical-kinetics-reaction scheme was used in the Williams et al. model. Williams et al. used an Arrhenius law for the decomposition reaction and an equilibrium law for the evaporative rate of the reactant.

Williams et al. [10] used an equilibrium relationship and a macroscopic energy balance to determine the surface temperature and surface concentration of the gaseous reactant. The use of the void

fraction also facilitated the weighting of thermal conductivity and heat capacity, which change by orders of magnitude from condensed phase to gas phase. Williams et al. assumed that pure nitramines would exhibit a "dark zone" similar to double-base propellants. They assumed this occurred at 1320 K and varied only slightly with pressure.

Kuo and Lu [12] proposed a detailed mathematical model for the liquid/bubble region of RDX combustion. They set forth equations of continuity, species, momentum, and energy for the liquid part in an Eulerian frame of reference. The governing equations for the gas portion were given for a single bubble in a Lagrangian frame of reference. They also reported relationships for specific surface area, pressure difference across the bubble interface, average bubble separation distance, average velocity of bubbles leaving a heated surface, average detachment bubble diameter, minimum heat flux necessary for bubble formation, void fraction at melt surface, and bubble formation rate. Many of these relationships require empirical parameters that have not been measured for propellant ingredients. Kuo and Lu did not solve their set of equations, and therefore, have no results to compare with the other research groups. Their model represents the first attempt to model the gas decomposition products in the propellant condensed phase as bubbles instead of a continuous gas void.

Ward et al [13]. solved the temperature equation for the condensed phase of HMX. They used a high activation energy assumption for the simple kinetic mechanism of $A \rightarrow B$, where A is the condensed species and B is the intermediate gas species, to obtain an approximate solution for the mass flux. This solution was first derived by Merzhanov [14].

They solved these equations along with simple energy and species equations for the gas phase. To match experimental data for HMX they needed to assume an activation energy of zero for the one global gas-phase reaction. This model does match the high experimental burning rate temperature sensitivity of HMX by using a gas-phase activation energy of zero. With this assumption the condensed-phase reaction zone plays an important role in determining the deflagration of HMX and demonstrates that this must be present in a detailed model to get calculations that match experimental σ_p values.

Over the last decade, several combustion models have been proposed for HMX and RDX using detailed chemical kinetic mechanisms [15–20]. They are all similar in their treatment of the gas phase. The continuity, energy, and species equations are solved in one dimension with species diffusion and temperature-dependent heat capacity and thermal conductivity. The use of a detailed chemical kinetic mechanism removes the need for empirical gas-phase global reactions or approximations. All use a variation from Brill's [21] two-step HMX and RDX decomposition mechanism in the condensed-phase region. The energy, continuity, and species
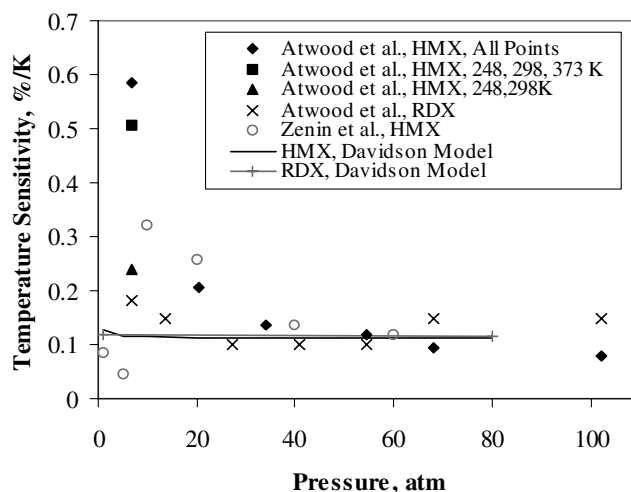

Fig. 2 σ_p **calculations with Davidson and Beckstead model compared with experimental data [22–24].**

Table 1 HMX physical property data

Property	Value (T in K)	Reference	Notes
H_f (kcal/mol)	17.92	Urbanski [26]	——
	21.03	Zierath et al. [27]	——
	24.54	DIPPR [25]	——
ρ (gm/cm^3)	1.87 (α form)	Akhavan [28]	Crystal at 20°C
	1.96 (β form)		
	1.82 (γ form)		
	1.78 (δ form)		
	$2.0046 - 0.0006 \cdot T$	Bedrov et al. [29]	Liquid density
	$2.5846 - 0.0015 \cdot T$	DIPPR	
T_m (K)	551	Hall [30]	——
	553.15	Maksimov [31]	
H_{pc} (Kcal/mol)	2.35	Hall	$\beta - \delta$
	16.7	Maksimov	Melting
	14.3	Sewell [32]	
	7.67	Zeman [33]	
	8.34	DIPPR	
λ (cal/cm/s/K)	$0.0015 - 1.15E - 06 \cdot T$	Parr [34]	HMX
	$5.28\text{E-}03 - 1.27\text{E-}05 \cdot T + 8.59\text{E-}09 \cdot T^2$	Bedrov et al.	Liquid
	$1.43\text{E-}03 - 1.06\text{E-}06 \cdot T$	DIPPR	
C_p (cal/g/K)	$4.97\text{E-}02 - 6.60\text{E-}04 \cdot T$	Parr	Solid
	$6.288\text{E-}02 - 6.09\text{E-}04 \cdot T$	Koshigoe [35]	
	0.395	Sewell	Liquid, 550 K
	$2.37\text{E-}01 + 3.57\text{E-}04 \cdot T$	DIPPR	Liquid
μ (poise)	$1.6335\text{E} + 32 \cdot T^{-11.552}$	Bedrov et al.	——
	$10 \cdot \text{Exp}(-11.752 + 3238.5/T)$	DIPPR	——
σ (dyne/cm)	$101.38 \cdot [1 - (T/T_c)]^{1.2222}$	DIPPR	——
T_{crit} (K)	1030	DIPPR	——
	927.15	Maksimov	——

Table 2 RDX physical property data

Property	Value (T in K)	Reference	Notes
H_f (kcal/mol)	14.69	LASL [36]	——
	14.83	DIPPR [25]	——
ρ (gm/cm^3)	1.82	Akhavan [28]	Crystal at 20°C
	$1.27 + 5.96\text{E-}04 \cdot T - 1.37\text{E-}06 \cdot T^2$	DIPPR	Liquid
T_m (K)	478.5	Hall [30]	——
H_{pc} (Kcal/mol)	8.52	Hall	Melting
	7.86	DIPPR	——
λ (cal/cm/s/K)	5.61E-04	DIPPR	Solid
	$1.52\text{E-}04 + 2.19\text{E-}07 \cdot T - 3.82\text{E-}10 \cdot T^2$	DIPPR	Liquid
C_p (cal/g/K)	$0.0309 + 7.03\text{E-}04 \cdot T$	Taylor [37]	Solid
	$4.73\text{E-}3 + 8.43\text{E-}4 \cdot T$	Parr	
	$0.213 + 4.43\text{E-}04 \cdot T$	DIPPR	Liquid
μ (poise)	$10 \cdot \text{Exp}(-13.713 + 3315.6/T)$	DIPPR	Liquid
σ (dyne/cm)	$53.161 \cdot [1 - (T/T_c)]^{1.1047}$	DIPPR	——
T_{crit} (K)	895.2	DIPPR	——
	840.15	Maksimov [31]	——

equations are also solved in the condensed-phase region. Two of these models used an evaporation condition to determine the location of the liquid-phase/gas-phase interface [15–18], and the other specified a surface temperature using experimental data [19,20].

All of the combustion models with detailed gas-phase kinetics have been able to calculate reasonable burning rates, temperature profiles, and species profiles. However, all did not predict the trends in burning-rate temperature sensitivity (σ_p) seen in experimental data for both HMX and RDX.

The experimental σ_p data [22–24] for HMX and RDX, along with σ_p calculations using the Davidson and Beckstead model are shown in Fig. 2. In this paper, all reported Davidson and Beckstead model calculations were done by the authors using the Design Institute for Physical Property Data (DIPPR) database [25][‡] thermodynamic and transport properties reported in Tables 1 and 2. Above 40 atm, HMX and RDX have similar σ_p values of ~0.1% K^{-1}. The experimental σ_p values for HMX increase to almost 0.6% K^{-1} for pressures less

than 20 atm if the higher temperature data are included, whereas the σ_p for RDX only increases to about 0.2% K^{-1}. Also, HMX σ_p has a dependence on initial temperature at low pressures. This can be seen in Fig. 2; the data measured at an initial temperature of 248 K and 298 K give an average σ_p of 0.24% K^{-1}. If the data taken at 373 K are included, then the average σ_p increases to 0.51% K^{-1}. Finally, the data taken at 423 K raise the average σ_p value to 0.59% K^{-1}. RDX σ_p does not have this dependence on initial temperature at low pressures. Two models [15,16,19,20] predict σ_p values of ~0.1% K^{-1} for both HMX and RDX notwithstanding the pressure. One model [17,18] predicts σ_p values for HMX that have the correct trend, but are less than experimental data values. However, this model predicts the σ_p values of RDX to be ~0.28% K^{-1}.

Experimental results, such as those shown in Fig. 3 from Bogg et al. [38], have confirmed that RDX and HMX both have bubbles in the thin melt-layer present during steady-state combustion. Parr and Hanson-Parr [39] noted that the liquid/gas surface was ill defined in HMX combustion at 1 atm because of the amount of bubbling present there. They also noted that HMX produced more bubbles than RDX.
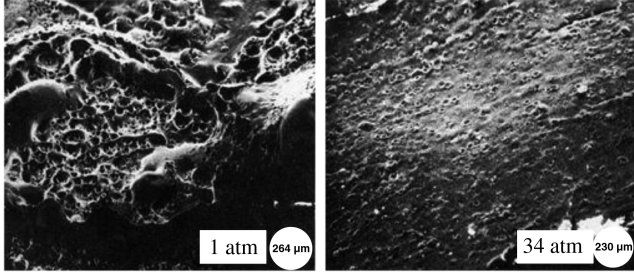

Fig. 3   Quenched samples of HMX displaying the reduction in bubble size with increasing pressure [38].

Glotov et al. [40] burned single crystals of RDX and noted that the bubbles only occupied 10% of the burning surface. It is hypothesized that one of the differences in HMX and RDX combustion that causes the divergent experimental σ_p values is the difference in bubble formation and bubble characteristics and how they affect the condensed-phase chemical kinetics. Previous attempts to simulate the bubbles present in HMX and RDX have modeled all the bubbles at one point in the numerical model as a void fraction having the same properties. For the research reported in this paper, the mathematical model used to simulate bubble behavior was modified to more accurately replicate the physical model.

Mathematical Model

The four-step condensed-phase kinetic mechanism developed by Brill [21] was used in this research. The species and energy equations were those used by Davidson and Beckstead [15]. The calculated mass flux was iterated until the heat flux from the gas phase matched that of the condensed phase at the gas/liquid boundary. More information on mass flux determination can be found in Davidson and Beckstead [15]. The next two sections detail the submodel used to calculate the bubble velocities.

Bubbly–Liquid Region

In the submodel, as the decomposition species are produced, it is assumed that only a part form bubbles. Even though the products are noncondensable gases, there is a small amount of these gases that is assumed to be dissolved in the liquid. The temperature of the system at this point is above their critical temperatures so that special methods must be used to describe their solubility. Prausnitz et al. [41] proposed expressions for the solubility of such gases, and they are shown in Eqs. (1) and (2). For simplicity, the activity coefficient γ_k is assumed to be one, and the fugacity f_{2V} is assumed to equal $P_g \cdot X_{g,k}$.

$$X\mathrm{sol}_{l,k} = f_{2V}/(f^o_{2,k}\gamma_k) \tag{1}$$

$$f^o_{2,k} = 7.224 - 7.534 T_{\mathrm{crit},k}/T - 2.598\, \ell n\,(T/T_{\mathrm{crit},k}) \tag{2}$$

Kuo and Lu [12] proposed a Lagrangian approach for RDX bubbles in 1993. In this section, a different Lagrangian approach is reported to calculate the bubble velocity and to simulate the formation of bubbles at various locations within the melt layer. In the submodel, once there are enough decomposition gases, mass is transferred from the liquid to form bubbles, which are grouped into packets of bubbles. All the bubbles in a packet have the same velocity throughout the liquid–bubble region calculation. The velocity profile for each group of bubbles is calculated using Eq. (3).

$$(\rho_g + C_{\mathrm{vm}}\rho_l)u_{\mathrm{bub}}V_{\mathrm{bub}}\frac{du_{\mathrm{bub}}}{dx} = F_B - F_D + F_{\mathrm{MG}} + F_{\mathrm{VM}} \tag{3}$$

The equation represents a force balance on the bubble. The first term on the right is the buoyancy force and is calculated by

$$F_B = V_{\mathrm{bub}}g(\rho_l - \rho_g) \tag{4}$$

The second term is the drag force and it is calculated by Eq. (5). The drag coefficient is assumed to be that for a rigid sphere in laminar flow [42] and is shown in Eq. (6).

$$F_D = \tfrac{1}{2}C_D\rho_l\pi(D_{\mathrm{bub}}/2)^2|u_{\mathrm{bub}} - u_l|(u_{\mathrm{bub}} - u_l) \tag{5}$$

$$C_D = (24/Re)(1 + 0.15Re^{0.687}) \tag{6}$$

The third term represents the Marangoni effect [43]. This effect occurs when a temperature gradient or a surfactant concentration gradient causes a surface tension gradient in the bulk fluid. Near the interface of the bubble and liquid, the motion is directed toward the region with larger surface tension. Since the liquid is incompressible, a bulk motion supported by a pressure gradient will develop in the opposite direction. The surface tensions of HMX and RDX decrease with increasing temperature [25], so that the Marangoni force is directed toward the higher temperatures. Gusachenko and Zarko [44] used the Marangoni effect to explain the lack of foam formation in some high-energetic materials until they are extinguished. They explain that this effect promotes the removal of the decomposition products into the gas phase. When the flame is extinguished, the temperature gradient decreases rapidly and the Marangoni effect is reduced dramatically. The remaining products cannot be removed rapidly enough and foam is formed. Nepomnyashchy et al. [43] and Margolis et al. [45] give similar equations for this force and they are shown in Eq. (7).

$$F_{\mathrm{MG}} = -\frac{\pi \cdot D^2_{\mathrm{bub}}}{\mathrm{fac}}\frac{d\sigma}{dT}\frac{dT}{dx}$$
$$\mathrm{fac} = (1 + \mu_l/\mu_g)(2 + \lambda_l/\lambda_g)$$
$$\mathrm{fac} = \rho_l/\rho_g \tag{7}$$

The first fac is the one used by Nepomnyashchy et al. and the second by Margolis et al. Both forms give similar results, and that from Nepomnyashchy et al. was used in the calculations reported in this paper.

The fourth term in Eq. (3) represents virtual mass. This force arises from the observation that the total force exerted by the liquid on the bubble, is in part, dependent on changes in the slip velocity. This force is a resistance to acceleration, which occurs because a portion of the liquid around the bubble acts as "added mass" and must be accelerated when the bubble accelerates [42]. The equation to describe the virtual-mass force is given by Eq. (8) [46]. The first term on the right appears on the left in Eq. (3). The virtual-mass coefficient is usually assumed to have a value of 0.5. [47]

$$F_{\mathrm{VM}} = -\rho_l C_{\mathrm{VM}} V_{\mathrm{bub}} u_{\mathrm{bub}}\frac{du_{\mathrm{bub}}}{dx} + \rho_l C_{\mathrm{VM}} V_{\mathrm{bub}} u_l \frac{du_l}{dx} \tag{8}$$

In this submodel, any pressure force is neglected because the pressure is assumed constant in the liquid. Lift force is also ignored because its calculation requires velocity components in at least two dimensions and this is a one-dimensional calculation. The initial velocity of each packet of bubbles is calculated using Eq. (9).

$$u_{\mathrm{bub},j} = M/\rho_g \tag{9}$$

The mass in each bubble packet remains constant throughout the calculation. The void fraction is determined using Eq. (10) and the liquid velocity is calculated from Eq. (11).

$$\phi = \sum_{j=1}^{\#\,\mathrm{bubble\ packets}} M_j/(\rho_g u_{\mathrm{bub},j}) \tag{10}$$

$$u_l = M_l/[\rho_l(1 - \phi)] \tag{11}$$

The initial bubble size is chosen for the specific pressure and ingredient based on experimental data. The gas density is calculated using the ideal gas relationship and liquid density is calculated with a temperature-dependent relationship. The pressure inside the bubble

is calculated by [48]:

$$P_g = (4\sigma + P_l D_{\text{bub}})/D_{\text{bub}} \tag{12}$$

Double-Precision Differential Algebraic Equation Solver Package (DDASPK) [49] is coupled with Double-Precision Variable-Coefficient ODE Solver (DVODE) [50] to solve the system of algebraic equations and ordinary differential equations. DDASPK is used to calculate the temperatures, species fractions, gas pressure, gas density, and liquid density. DVODE integrates the bubble-velocity equations with lagged properties to supply DDASPK with bubble velocities and void fractions. The system of equations is solved until either a gas surface condition is met, or the void fraction reaches that which would form foam.

Foam Region

In RDX and HMX, it is assumed that bubbles are formed through their nucleation in a liquid that is supersaturated. This method of bubble production can produce fairly homogenous bubble sizes that grow consistently as they rise to the surface [48]. As long as the void fraction is below a critical value, the system can be modeled as having a continuous liquid phase surrounding individual bubbles. For values greater than the critical void fraction, foam is formed. The critical void fraction for monodisperse-disordered foams identified with the Bernal packing density of hard spheres is ≈0.64 [48]. Foam can be categorized as wet foam or dry foam. Dry foam is defined as one having a large void fraction, > ∼ 0.98, whereas wet foam is one having a smaller void fraction. It is assumed that the foam encountered in RDX and HMX is wet foam.

In foam, the bubbles are pushed together leaving thin films to separate them. The majority of the liquid is located in channels of finite width bordering the bubbles called Plateau borders [36]. There is no continuous liquid phase in the foam. As the bubbles get closer together, the larger bubbles will grow at the expense of any smaller bubbles. This phenomenon is referred to as Ostwald Ripening [51].

The following is the portion of the liquid–bubble submodel developed to describe the physical processes explained in the first part of this section. In the submodel, the foam region begins in the calculation when ϕ_{crit} is reached. The temperature and species equations are solved in the same manner as for the liquid–bubble region. However, when the critical void fraction is reached, Eq. (3) no longer applies because it was derived for a continuous liquid phase. Foams are three-dimensional phenomena that would require large amounts of computational time to model rigorously. This is beyond the scope of this model and only general characteristics of foams are simulated.

In the physical process, once foam is formed, the drag force on the bubbles will be significantly reduced because there is not a continuous liquid phase. The momentum imparted from the newly formed gas should then speed up the bubble velocity. If the velocities of the bubbles increase faster than the rate mass is added to the bubble phase, the void fraction decreases. However, if the void fraction were to go below the critical void fraction, drag would come into play and slow down the bubbles, increasing the void fraction. Furthermore, in order for $\phi_{\text{foam}} > \phi_{\text{crit}}$, a force must be applied to drive out the liquid [48]. To model this mathematically, it is assumed that all of these factors counterbalance each other to maintain $\phi_{\text{foam}} = \phi_{\text{crit}}$ until decomposition and evaporation have depleted the remaining liquid [see Eq. (13)].

$$\phi_{\text{foam}} = \phi_{\text{crit}} \quad \text{if } \phi_{\text{crit}} \geq M_g/M$$
$$\phi_{\text{foam}} = M_g/M \quad \text{if } \phi_{\text{crit}} < M_g/M \tag{13}$$

The next equation is implemented to model the physical process of Ostwald Ripening. In the submodel, when the foam region is reached, the total bubble number flux is calculated using Eq. (14).

$$\text{FLUX}_{\text{bub}} = \sum_{j=1}^{\text{\# bubble packets}} M_j \Bigg/ \left(\frac{\pi}{6} D_{\text{bub}}^3 \rho_g\right) \tag{14}$$

In the foam, new mass added to the bubble phase will increase the size of the bubbles already present instead of producing new bubbles. Thus, the bubble number flux is assumed to remain constant throughout the foam region. The volume and diameter of a bubble in the foam region is computed using Eq. (15).

$$V_{\text{bub}} = \frac{\pi}{6} D_{\text{bub}}^3 = M_g/\text{FLUX}_{\text{bub}}\rho_g \tag{15}$$

In the physical process, it is assumed that the thin films that separate the bubbles in the foam would have an inhibited evaporation rate because there are surface tension forces on both sides of the film. As the foam gets frothier, more of the surface area of the bubble comes from those thin films and the area available for evaporation decreases. To model this, as an initial approximation, evaporation is neglected in the foam region.

In the foam region, the submodel uses DDASPK as the solver and stops at the gas surface conditions given by Eqs. (16) and (17). In Eq. (17), the value of r, dT_s/dT_o, is experimentally measured by Zenin [23].

$$(1 - \phi)u_l\rho_l = q_{\text{evap}} \quad \text{at } T_o = 298 \text{ K} \tag{16}$$

$$T_s = T_s|_{T_o=298\text{ K}} + r(T_o - 298 \text{ K}) \tag{17}$$

Using Zenin's experimental data to fix the surface temperature is the same approach used by Prasad et al. [19,20] in their combustion model with detailed gas-phase chemical kinetic mechanisms. The evaporation relationship used in the other two models [15–18] is applicable to bubbly/liquid interfaces, but not that of a foam. A foam break-up model would be needed to accurately predict the surface temperature of HMX. This was beyond the scope of this initial model and Zenin's experimental data were used for the surface temperature.

Input Transport and Thermodynamic Properties

Tables 1 and 2 summarize a representative sample of the transport and thermodynamic property data reported for HMX and RDX. The majority of the values were found through the DIPPR database [25]. For consistency, the DIPPR values were used in the calculations for this paper.

Figure 4 gives the initial bubble diameters used for both HMX and RDX. The bubble diameter at 1 atm came from an approximation of the bubble diameters in Fig. 3. At pressures the bubble diameters were assumed to be slightly less than the length of the calculated melt layer.
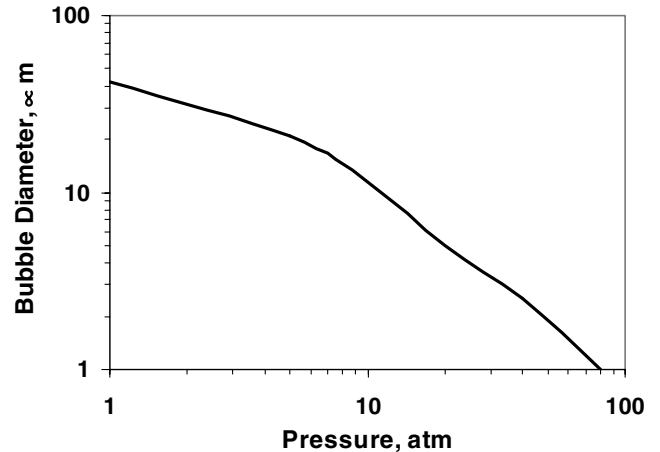

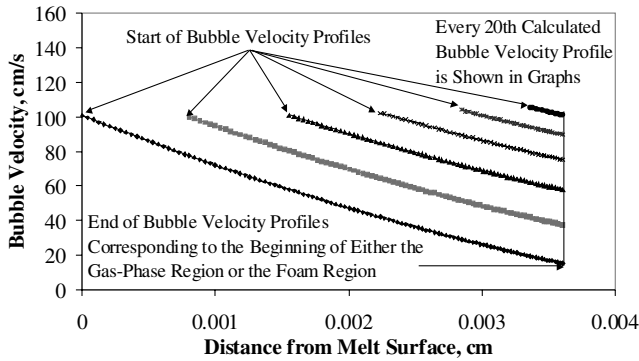**Fig. 4 Initial bubble diameter used in liquid–bubble submodel for HMX and RDX.**
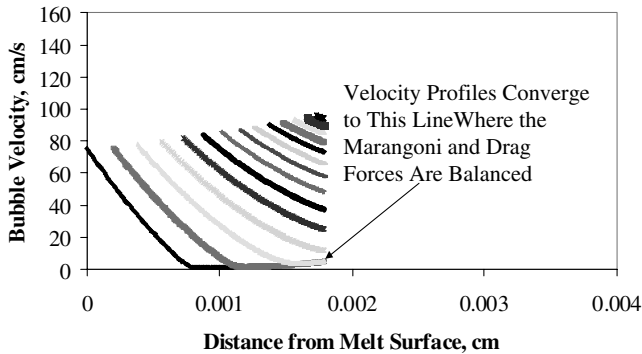
Fig. 5   Bubble-velocity profiles for HMX at 1 atm.

Fig. 6   Bubble-velocity profiles for HMX at 5 atm.

Results

Velocity Calculations

In the liquid–bubble submodel, as mass is transferred to the gas phase, the mass is grouped into packets of bubbles that are assigned the same velocity throughout the calculation. To get the results reported in this section, the mass transferred to the bubble phase for each 0.5 K of the calculation was grouped together as a packet. Calculations showed that a smaller interval of temperature in the calculation would not change the results, but would slow down the calculation. Also, an interval of temperature was used instead of distance because at high pressures, where the liquid–bubble region is small, greater resolution of the velocity profiles was desired. Since the temperature gradient is steeper at high pressures, the distance between the start of the mass packets was shorter in the calculations at higher pressures.

The velocity profiles at 1 and 5 atm are shown in Figs. 5 and 6. The figures are shown with the same axes for comparison between the pressures. The velocity profiles are given versus the distance from the melt surface. Every 20th calculated bubble-velocity profile is shown in the figures. The initial velocities were determined by the total mass flux divided by the gas density. The gas density changed and so the initial velocity of the profiles changed. The end of the velocity profiles corresponded to whichever came first, a liquid-volume

fraction of 0.36 where the foam submodel was used, or the beginning of the droplet-gas region.

The distance between the start of the profiles indicates the temperature gradient at that point. In the calculations, as the pressure increased, the diameter of the bubbles decreased, and the initial drag per volume on the bubbles increased. The drag force per volume is roughly proportional to the inverse of the square of the bubble diameter. Thus, there was the rapid decrease in the slope of the velocity profiles as the pressure increased.

The calculations indicated that the final velocity, at which the Marangoni effect and the drag force were balanced, increased with pressure. This velocity can be termed the terminal velocity and is the velocity to which the different bubble packet velocities converge. Holding the pressure constant, the terminal velocity increased as the temperatures increased. At 1 atm the drag was not great enough to achieve such a velocity. The final calculated terminal velocity at 5 atm was 5 cm/s and at 80 atm was 24 cm/s. This mainly occurred for two reasons. First, the temperature gradient was much higher at high pressures, and so the surface tension gradient was much higher, causing the Marangoni effect to be greater. Second, as the pressure increased the surface temperature increased and the viscosity of the liquid decreased, reducing the drag force. These two phenomena were somewhat balanced by the decrease in bubble size in the HMX calculations. If this did not happen, the bubble velocities in the calculations would increase rapidly. Of the pressures studied, 80 atm was the only pressure where the calculated gas volume fraction did not reach the necessary value, 0.64, signifying the start of the foam region. The 80 atm calculation also had the largest Marangoni force. This agrees qualitatively with the observations of Gusachenko and Zarko [44] that were discussed previously.

The calculated temperature profiles in the liquid are shown in Fig. 7 for HMX. The greatest relative difference in the calculated temperature gradients between different initial temperatures occurred at 1 atm. At 1 atm, between the two initial temperature cases, the 423 K case had the steeper calculated temperature gradient. It is interesting to note how the relative temperature-gradient difference changed with pressure. From 1 atm to 10 atm the difference in temperature gradient between initial temperatures decreased. By 20 atm the 298 K case had a slightly steeper temperature gradient. In the numerical model, the Marangoni force is proportional to the temperature gradient. Therefore as the pressure increased, the greater Marangoni force switched from the higher initial temperatures to the lower ones.

Burning-Rate Temperature Sensitivity Calculations

The σ_p values calculated for this report were computed using Eq. (18). The mass fluxes used in Eq. (18) were those calculated using the computational model with initial temperatures of 423 and 298 K.

$$\sigma_p = \frac{\ln[(M|_{423\,K})/(M|_{298\,K})]}{423\,K - 298\,K} \tag{18}$$

Using the liquid–bubble submodel dramatically improved the agreement between the calculated HMX σ_p values and the experimentally measured values. Figure 8 reports results of the
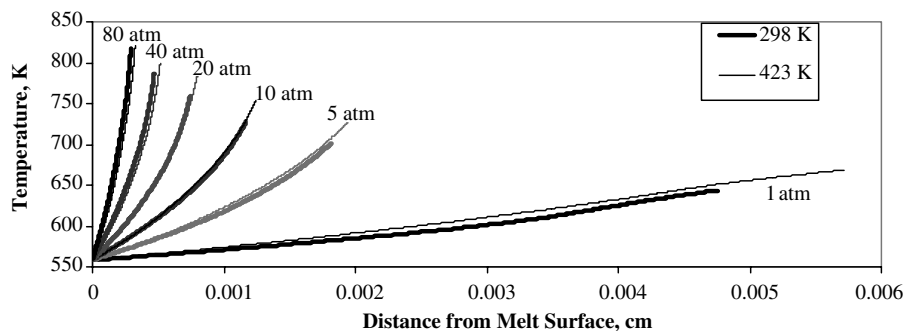

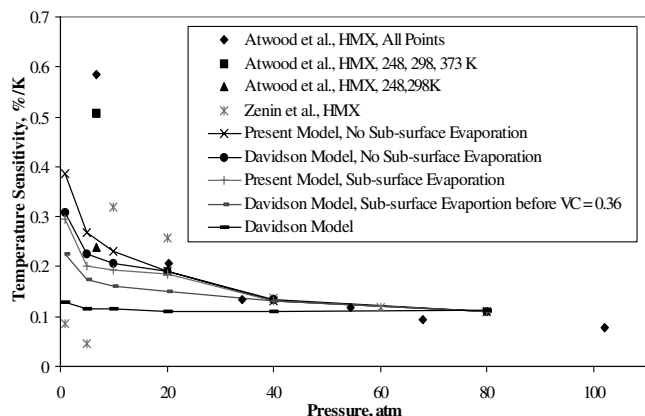Fig. 7   Calculated HMX liquid temperature profiles.

Fig. 8 Effect of different aspects of the liquid–bubble submodel on calculated HMX σ_p values [22–24].

parametric study to see what parts of the submodel were responsible for the improvement.

As shown in the figure, a consistent trend in calculated σ_p was achieved with the Davidson model by stopping the subsurface evaporation after the liquid-volume fraction reached 0.36, which corresponded to the start of a foam region. As explained earlier, the structure of the foam might reduce the available surface area for evaporation and make this assumption valid. However, the calculated σ_p values were still lower than the measured ones.

Using the liquid–bubble submodel, the calculated σ_p values increased even more than those calculated after subsurface evaporation was removed or limited in the Davidson model. This occurred because the calculated temperature gradients were steeper at higher initial temperatures at low pressures. This caused the higher initial temperature cases to have a greater Marangoni force. Thus, the bubble velocities decreased more slowly with a greater Marangoni force, and the liquid velocities were smaller than those calculated with a lesser Marangoni force. Therefore, the liquid had a greater residence time inside the melt and greater time to decompose. The increased decomposition increased the calculated burning rate in cases with a greater Marangoni force.

By removing all of the subsurface evaporation, the calculated σ_p values increased even more for both the Davidson model and the present model. However, the calculated burning rate at 298 K increased 6.5% when subsurface evaporation was removed in the Davidson model, overpredicting the experimental data. When using the present model without subsurface evaporation the calculated burning rate at 298 K only increased 1.5% and gave the calculated σ_p values closest to experimental data.

The effect of subsurface evaporation on the liquid-volume fraction of HMX is shown graphically in Fig. 9. The Davidson model with no subsurface evaporation had the same liquid-volume-fraction profile for the different initial temperatures, but the one at 423 K extended to a liquid-volume fraction about 50% lower. In the Davidson model, the mass flux of the liquid and gas phases were equal and constant, so that without evaporation, the fraction of the HMX decomposed was
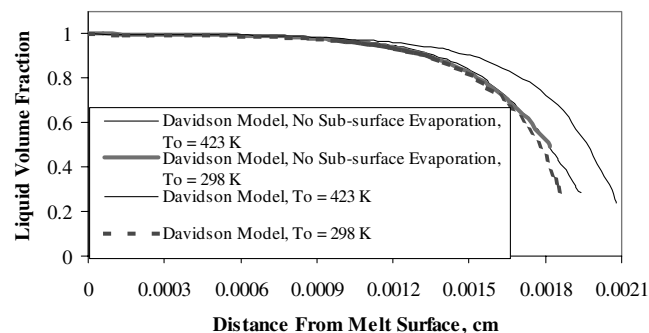

Fig. 9 Effect of subsurface evaporation on liquid-volume fraction of HMX at 5 atm.
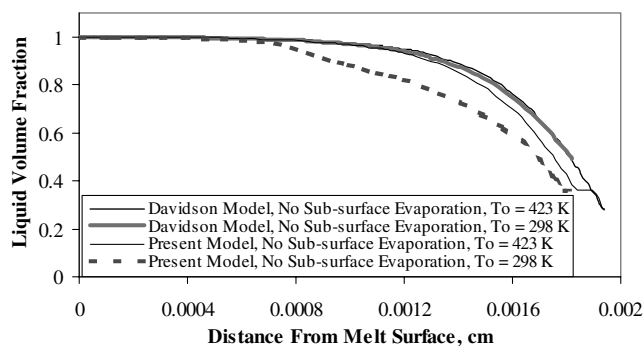

Fig. 10 Effect of liquid–bubble submodel on liquid-volume fraction of HMX at 5 atm.

equal to one minus the liquid-volume fraction. Thus, at the higher initial temperatures there was significantly more decomposition and higher calculated burning rates, which increased the calculated σ_p values.

The liquid-volume fraction profile with subsurface evaporation at 298 K followed those without subsurface evaporation until the final 2 mm of the melt. At this point, the slope of the line decreased rapidly as the evaporation sped up. Because the calculated melt thickness in the 423 K cases was greater, there was even more calculated subsurface evaporation. This increased the calculated heat flux at the end of the melt, and the computed burning rate was reduced. This further increased the melt-layer thickness and more evaporation was calculated and the calculated burning rate was reduced even more. As can be seen in Fig. 9, there was little difference in the final liquid-volume fraction between the two initial temperatures (with subsurface evaporation), and so there would be little difference in their liquid-phase decomposition. Thus, their calculated burning rates would be similar and the calculated σ_p values low.

Figure 10 shows the effect of the liquid–bubble submodel on the liquid-volume fraction of HMX at low pressures. Subsurface evaporation was excluded to focus on the effect of adding the liquid–bubble submodel. The Davidson-model liquid-volume-fraction profiles fell on top of each other, whereas the present model profiles were separated. The difference in the present model profiles arose from the difference in bubble velocities at the different initial temperatures. The higher initial temperature calculations had higher liquid temperature gradients and greater Marangoni forces on the bubbles. The bubbles slowed down less, and the liquid-volume fraction remained higher. Therefore, the liquid had a greater residence time at higher initial temperatures and therefore had more decomposition. This increased the calculated σ_p values.

At higher pressures, as at lower pressures, the calculated melt-layer thickness was greater at higher initial temperatures. This led to more decomposition at the higher initial temperatures and a greater burning rate. In opposition to this, the calculated Marangoni forces were greater at the lower initial temperatures at the higher pressures, which would make the calculated burning rates higher at lower initial temperatures. However, the calculated σ_p values remained positive at the higher pressures because the difference in melt-layer thickness had a greater effect than the difference in Marangoni forces on the calculated burning rates.

For both the Davidson model and the present model, no increase was evident in the calculated σ_p values without using the surface conditions defined in Eqs. (16) and (17). Equation (17) is dependent on the experimentally determined surface-temperature data from Zenin [23]. To perform a more predictive calculation of the surface temperature, multidimensional modeling of the foam would need to be done to determine the available surface area for evaporation. Because this is beyond the scope of the 1-D model, Eq. (17) was built into the submodel. However, it is important to note that the increase in surface temperature with the increase in initial temperature is necessary to calculate σ_p values similar to experimental ones.

The results of a parametric study calculating RDX σ_p values, similar to the study calculating HMX σ_p values, are shown in Fig. 11.
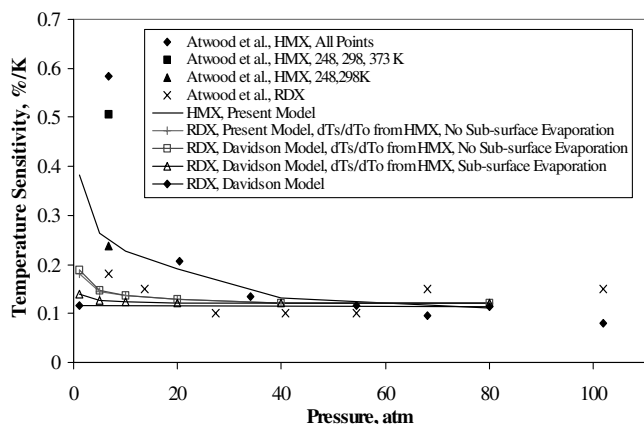
Fig. 11   Calculated σ_p values for RDX and HMX compared with experimental data [22–24].

Reducing the evaporation in the subsurface calculations increased the computed RDX σ_p values, but not to the same extent as for HMX. The addition of the liquid–bubble submodel had minimal effect on the calculated RDX σ_p. This was the desired result. As can be seen in Fig. 11, the experimental σ_p values increase at low pressures, but to a lesser degree than for HMX. The calculated σ_p values with no subsurface evaporation had the same trend. A major difference between the HMX and RDX calculations was that there were substantially fewer decomposition gases produced in RDX subsurface combustion. Thus, the total condensed phase did not have a large effect on the RDX calculation of σ_p. Hence, the present model is able to differentiate σ_p between RDX and HMX.

In the present model, Brill's [21] condensed-phase kinetic mechanism is used. None of the kinetic parameters or physical properties were "adjusted" to get higher σ_p values. As seen in Fig. 11, the calculated σ_p values at pressures below 10 atm are still less than the experimentally measured ones. Increasing the exothermicity of the condensed-phase kinetic mechanism would increase the σ_p values. The difference of exothermicity in the condensed phase of HMX and RDX at low pressures causes the difference in their σ_p values [52]. The improvements in the bubble/foam model permitted the exothermic differences to occur. Also, below 30 atm a value of 0.2 was used for Zenin's [23] r parameter. He has measured values up to 0.26 for this parameter at low pressures. Increasing the value of the r parameter at low pressures would increase the calculated σ_p values even more. Furthermore, σ_p is a derivative property. It is determined experimentally by the difference of measured burning rates. Any experimental error in the burning-rate measurement will be compounded when calculating σ_p. The actual σ_p values at low pressures could be less than those reported.

Previously, the two assumptions for calculating the bubble velocity have been $\rho_g u_b = M$ and $u_b = u_l$ [45]. It has been shown that $\rho_g u_b = M$ is a better assumption and it was used in all of the previous combustion models with detailed gas-phase kinetics. An important conclusion from this work is that at low pressures, neither assumption is valid for HMX, and their use will adversely effect the calculations. The actual bubble velocities lie somewhere between those calculated using the two assumptions.

Conclusion

Calculations with the liquid–bubble submodel produced the desired trends in both the HMX and RDX calculated σ_p values. To predict consistent HMX σ_p values with the model, first, evaporation in the subsurface was limited near the gas/liquid surface. Second, the difference in surface temperature at different initial temperatures had to follow experimental data. Third, the Marangoni effect was added to the calculation of the bubble velocities. At low pressures, the Marangoni effect is greater in the higher initial temperature calculations because the temperature gradient is steeper, and this

increases the burning rate. In the RDX calculations there was little change in the calculated σ_p values with the addition of the submodel.

References

[1]   Parr, R. G., and Crawford, B. L., "A Physical Theory of Burning of Double Base Rocket Propellants: Part 1," *Journal of Physical and Colloid Chemistry*, Vol. 54, No. 6, 1950, pp. 929–954.

[2]   Rice, O. K., and Ginell, R., "The Theory of the Burning of Double Base Rocket Powders," *Journal of Physical and Colloid Chemistry*, Vol. 54, No. 6, 1950, pp. 885–917.

[3]   Wilfong, R. E., Penner, S. S., and Daniels, F., "An Hypothesis for Propellant Burning," *Journal of Physical and Colloid Chemistry*, Vol. 54, No. 6, 1950, pp. 863–872.

[4]   Hermance, C. E. "A Model of Composite Propellant Combustion Including Surface Heterogeneity and Heat Generation," *AIAA Journal*, Vol. 4, No. 9, 1966, pp. 1629–1637.

[5]   Beckstead, M. W., and McCarty, K. P., "Calculated Combustion Characteristics of Nitramine Monopropellants," CPIA Publication 281, 1976, pp. 58–67.

[6]   Cohen, N. S., "Review of Composite Propellant Burn Rate Modeling," *AIAA Journal*, Vol. 18, No. 3, 1980, pp. 277–293.

[7]   Ben-Reuven, M., Caveny, L. H., Vichnevestsky, R., and Summerfield, M., "Flame Zone and Sub-Surface Reaction Model for Deflagrating RDX," *Proceedings of the 16th Symposium (International) on Combustion*, The Combustion Institute, Pittsburgh, PA, 1976, pp. 1223–1233.

[8]   Ben-Reuven, M., and Caveny, L. H., "Nitramine Flame Chemistry and Deflagration Interpreted in Terms of a Flame Model," *AIAA Journal*, Vol. 19, No. 10, 1981, pp. 1276–1285.

[9]   Mitani, T., and Williams, F. A., "A Model for the Deflagration of Nitramines," *Proceedings of the 21st Symposium (International) on Combustion*, The Combustion Institute, Pittsburgh, PA, 1986, pp. 1965–1974.

[10]   Li, S. C., Williams, F. A., and Margolis, S. B., "Effects of Two-Phase Flow in a Model for Nitramine Deflagration," *Combustion and Flame*, Vol. 80, No. 3-4, 1990, pp. 329–349.

[11]   Margolis, S. B., Williams, F. A., and Armstrong, R. C., "Influences of Two-Phase Flow in the Deflagration of Homogeneous Solids," *Combustion and Flame*, Vol. 67, No. 3, 1987, pp. 249–258.

[12]   Kuo, K. K., and Lu, Y. C., "Modeling of Physicochemical Processes of Burning RDX Monopropellants," *Proceedings of the 30th JANNAF Combustion Meeting*, Vol. 2, CPIA Publication 606, Chemical Propulsion Information Agency, Columbia, Maryland, 1993, pp. 235–257.

[13]   Ward, M. J., Son, S. F., and Brewster, M. Q., "Steady Deflagration of HMX with Simple Kinetics: A Gas Phase Chain Reaction Model," *Combustion and Flame*, Vol. 114, No. 3-4, 1998, pp. 556–568.

[14]   Merzhanov, A. G., "The Theory of Stable Homogeneous Combustion of Condensed Substances," *Combustion and Flame*, Vol. 13, No. 2, 1969, pp. 143–156.

[15]   Davidson, J. E., and Beckstead, M. W., "Improvements to Steady-State Combustion Modeling of Cyclotrimethylenetrinitramine," *Journal of Propulsion and Power*, Vol. 13, No. 3, 1997, pp. 375–383.

[16]   Davidson, J. E., and Beckstead, M. W., "A Three-Phase Model of HMX Combustion," *26th Symposium (International) on Combustion*, The Combustion Institute, Pittsburgh, Pennsylvania, 1996, pp. 1989–1996.

[17]   Liau, Y., and Yang, V., "Analysis of RDX Monopropellant Combustion with Two-Phase Subsurface Reactions," *Journal of Propulsion and Power*, Vol. 11, No. 4, 1995, pp. 729–739.

[18]   Kim, E. S., Yang, V., and Liau, Y.-C., "Modeling of HMX/GAP Pseudo-Propellant Combustion," *Combustion and Flame*, Vol. 131, No. 3, 2002, pp. 227–245.

[19]   Prasad, K., Yetter, R. A., and Smooke, M., "An Eigenvalue Method for Computing the Burning Rates of RDX Propellants," *Combustion Science and Technology*, Vol. 124, No. 1–6, 1997, pp. 35–82.

[20]   Prasad, K., Yetter, R. A., and Smooke, M. D., "An Eigenvalue Method for Computing the Burning Rates of HMX Propellants," *Combustion and Flame*, Vol. 115, No. 3, 1998, pp. 406–416.

[21] Brill, T. B., "Multiphase Chemistry Considerations at the Surface of Burning Nitramine Monopropellants," *Journal of Propulsion and Power*, Vol. 11, No. 4, 1995, pp. 740–751.

[22] Atwood, A. I., Boggs, T. L., Curran, P. O., Parr, T. P., Hanson-Parr, D. M., Price, C. F., and Wiknich, J., "Burning Rate of Solid Propellant Ingredients, Part 2: Determination of Burning Rate Temperature Sensitivity," *Journal of Propulsion and Power*, Vol. 15, No. 6, 1999, pp. 748–752.

[23] Zenin, A. A., Puchkov, V. M., and Finyakov, S. V., "Characteristics of HMX Combustion Waves at Various Pressures and Initial Temperatures," *Combustion, Explosion and Shock Waves*, Vol. 34, No. 2, 1998, pp. 170–176.

[24] Zenin, A. A., Finjakov, S. V., Puchkov, V. M., and Ibragimov, N. G., "Temperature and Pressure Sensitivities of Burning Wave Parameters of Nitramine-Containing Propellants and HMX," *Journal of Propulsion and Power*, Vol. 15, No. 6, 1999, pp. 753–758.

[25] Design Institute for Physical Property Data (DIPPR), Project 801.

[26] Urbanski, T., *Chemistry and Technology of Explosives*, Vol. 4, Pergamon Press, Oxford, 1984, pp. 605–610.

[27] Zierath, J., Licht, H. H., and Krien, G., "Thermochemische Untersuchungen an Nitraminen," *Thermochimica Acta*, Vol. 6, No. 5, 1973, pp. 465–472.

[28] Akhavan, J., *The Chemistry of Explosives*, Royal Society of Chemistry Information Services, Cambridge, England, 1998, pp. 39–40.

[29] Bedrov, D., Smith, G. D., and Sewell, T. D., "Thermal Conductivity of Liquid Octahydro-1,3,5,7-tetranitro-1,3,5,7-tetrazocine (HMX) from Molecular Dynamics Simulations," *Chemical Physics Letters*, Vol. 324, No. 1–3, 2000, pp. 64–68.

[30] Hall, P. G., "Thermal Decomposition and Phase Transition in Solid Nitramines," *Transactions of the Faraday Society*, Vol. 67, No. 3, 1971, pp. 556–562.

[31] Maksimov, Y. Y., "Boiling Point and Enthalpy of Evaporation of Liquid Hexogen and Octogen," *Russian Journal of Physical Chemistry*, Vol. 66, No. 2, 1992, pp. 280–281.

[32] Sewell, T. D., and Menikoff, R., "Constituent Properties of HMX Needed for Meso-scale Simulations," Los Alamos National Laboratory, LA-UR-00-3804-rev, Los Alamos, New Mexico, 2001.

[33] Zeman, S., "Some Predictions in the Field of the Physical Thermal Stability of Nitramines," *Thermochimica Acta*, Vol. 302, No. 1–2, 1997, pp. 11–16.

[34] Parr, T. P., and Hanson-Parr, D. M., "Thermal Properties Measurements of Solid Rocket Propellant Oxidizers and Binder Materials as a Function of Temperature," *Journal of Energetic Materials*, Vol. 17, No. 1, 1999, pp. 1–47.

[35] Koshigoe, L. G., Shoemaker, R. L., and Taylor, R. E., "Specific Heat of HMX," *AIAA Journal*, Vol. 22, No. 11, 1984, pp. 1600–1601.

[36] *LASL Explosive Property Data*, edited by T. R. Gibbs and A. Popolato, University of California Press, Berkeley, California, 1980, pp. 203–223.

[37] Shoemaker, R. L., Stark, J. A., and Taylor, R. E., "Thermophysical Properties of Propellants," *High Temperatures High Pressures*, Vol. 17, No. 4, 1985, pp. 429–435.

[38] Boggs, T. L., Price, C. F., Zurn, D. E., Derr, R. L., and Dibble, E. J., "The Self Deflagration of Cyclotetramethylenetetranitramine (HMX)," AIAA Paper 77-859, 1977.

[39] Parr, T. P., and Hanson-Parr, D. M., "HMX Ignition and Combustion Flame Structure," *Proceedings of the 34th JANNAF Combustion Subcommittee Meeting*, Publication 662, Vol. 2, Chemical Propulsion Information Agency, Columbia, Maryland, 1997, pp. 481–490.

[40] Glotov, O. G., Karasev, V. V., Zarko, V. E., and Svit, A. G., "Burning of Single Crystals and Pressed Tablets of RDX," *Energetic Materials, Reactions of Propellants, Explosives, and Pyrotechnics, Proceedings of 34th International Annual Conference of ICT*, Institut Chemische Technologie, Karlfruhe, Germany, 2003, pp. 47-1–47-15.

[41] Prausnitz, J. M., Anderson, T. F., Grens, E. A., Eckert, C. A., Hsieh, R., and O'Connell, J. P., *Computer Calculations for Multicomponent Vapor-Liquid and Liquid-Liquid Equilibria*, Prentice–Hall, Englewood Cliffs, New Jersey, 1980, pp. 55.

[42] Delnoij, E., Lammers, F. A., Kuipers, J. A., and van Swaaij, W. P., "Dynamic Simulation of Dispersed Gas-Liquid Two-Phase Flow Using a Discrete Bubble Model," *Chemical Engineering Science*, Vol. 52, No. 9, 1997, pp. 1429–1458.

[43] Nepomnyashchy, A. A., Velarde, M. G., and Colinet, P., *Interfacial Phenomena and Convection*, Chapman & Hall/CRC, Boca Raton, FL, 2002, pp. 39–91.

[44] Gusachenko, L. K., and Zarko, V. E., "The Marangoni Effect in Combustion of Energetic Materials with a Liquid Surface Layer," *Combustion, Explosion and Shock Waves*, Vol. 32, No. 2, 1996, pp. 239–240.

[45] Margolis, S. B., Williams, F. A., and Armstrong, R. C., "Influences of Two-Phase Flow in the Deflagration of Homogeneous Solids," *Combustion and Flame*, Vol. 67, No. 3, 1987, pp. 249–258.

[46] Guo, D., and Irons, G. A., "Modeling of Gas-Liquid Reactions in Ladle Metallurgy, Part 2: Numerical Simulation," *Metallurgical and Materials Transactions B: Process Metallurgy and Materials Processing Science*, Vol. 31B, No. 6, 2000, pp. 1457–1464.

[47] Mortensen, G. A., and Trapp, J. A., "Two-Phase Flow Modeling with Discrete Particle," *Two-Phase Flow in Energy Exchange Systems*, edited by M. S. Sohal and T. J. Rabas, Vol. 220, Heat Transfer Division Series, The American Society of Mechanical Engineers, New York, 1992, pp. 73–85.

[48] Weaire, D., and Hutzler, S., *The Physics of Foams*, Clarendon Press, Oxford, 1999, pp. 39–48.

[49] Petzold, L. R., "A Description of DASSL: A Differential/Algebraic System Solver," *Scientific Computing: Applications of Mathematics and Computing to the Physical Sciences*, edited by R. S. Stepleman, North–Holland, Amsterdam, 1983, pp. 65–68.

[50] Brown, P. N., Byrne, G. D., and Hindmarsh, A. C., "VODE: A Variable Coefficient ODE Solver," *SIAM Journal on Scientific and Statistical Computing*, Vol. 10, No. 5, 1989, pp. 1038–1051.

[51] Walstra, P., "Principles of Foam Formation and Stability," *Foams: Physics, Chemistry and Structure*, edited by A. J. Wilson, Springer–Verlag, London, 1989, pp. 6.

[52] Washburn, E. B., Beckstead, M. W., Hecker, W. C., Howe, J., and Waroquet, C., "Modeling Condensed Phase Kinetics and Physical Properties in Nitramines: Effects on Burning Rate Temperature Sensitivity," *Proceedings of the 37th JANNAF Combustion Subcommittee Meeting*, Publication 701, Vol. 1, Chemical Propulsion Information Agency, Columbia, Maryland, 2000, pp. 309–318.